MATERIALS CHEMISTRY
FRONTIERS

RESEARCH ARTICLE

View Article Online
View Journal | View Issue

Cite this: *Mater. Chem. Front.*, 2024, **8**, 1844

MXene composite with Ni/Co sulfide for enhanced hydrogen evolution reaction†

Mohit Kumar,‡ Bhimanaboina Ramulu ‡ and Jae Su Yu *

To produce clean and green hydrogen energy from electrolytic water, better electrocatalytic materials need to be developed. Herein, we reported the development of a Ti_3C_2 MXene@Ni/Co sulfide hybrid material for the use in hydrogen evolution reaction (HER) process, which is effective and stable. The shape of metal sulfide and its interactions with Ti_3C_2 MXene caused electronic coupling. This increased both the exposed metal sulfide's active edge sites and the charge-transfer speed. When compared with pure MXene and Ti_3C_2 MXene@NiS nanostructure, Ti_3C_2 MXene@Co_4S_3 exhibited outstanding electrocatalytic activity and stability in the HER process. The unique properties of the skeletal structure and the robust interface interaction between Co_4S_3 and MXene are responsible for the superior performance of Ti_3C_2 MXene@Co_4S_3 in the HER process. Our research offers a practical method to synthesize specialized nanostructures for electrocatalysis, electronics, and other applications.

Received 4th February 2024,
Accepted 22nd February 2024

DOI: 10.1039/d4qm00095a

rsc.li/frontiers-materials

1. Introduction

The need to develop clean and green energy is driven by increasing concerns about the environment related to the unrestrained use of fossil fuels and energy problems caused by population growth. The development of future green energy and the environmental-friendly generation of hydrogen as a source of energy could both be achieved through the breakdown of water, powered by renewable energy.[1–3] A hydrogen or oxygen evolution reaction (HER or OER) can occur during the water decomposition process, and Ir, Ru, and Pt catalysts are commonly used for both such reactions. When it comes to the widespread industrialization of water electrolysis, the use of expensive precious metals is not a feasible option.[4–6] Consequently, it is necessary to use catalysts that are extremely effective, reliable, and affordable. Nitrides,[7] transition metal oxides,[8] phosphides,[9] sulfides,[10] and selenides[11] are among the non-precious metallic materials that have been developed to act as effective electrocatalysts. The enhanced electrocatalyst design is anticipated to benefit from the use of transition metal dichalcogenides (TMDs)[6] which have been identified as an important series of electrocatalysts with high conductivities, which can be synthesized *via* simple processing methods. Nickel sulfide,[12] cobalt sulfide,[13] molybdenum sulfide,[14] and iron sulfide[15] are among the non-precious metal electrocatalysts based on layered TMDs currently being studied concerning their application in general water decomposition. The distinctive structural characteristics of TMD catalysts, such as their structural disorder, capacity for doping with foreign metals, and morphological control, are responsible for their enhanced electrocatalytic activity in the HER and OER processes.[16] Due to their affordability, high activity, and simple synthesis process, nickel- and cobalt-based compounds have drawn the most attention.[17] For the HER and OER, for instance, a Ni–FeS_2 lattice on Ni foam results in improved catalytic activity.[18]

The electrocatalytic activity of TMDs can be enhanced by adding a conductive material to them, which leads to variations in the ΔGH^* and the electrical conductivity, as determined using density functional theory (DFT) calculations.[16,19] In this regard, a variety of catalyst supports, such as reduced graphene oxide,[20] multi-walled carbon nanotubes,[21] and other carbon-based materials,[22] have been investigated. However, the majority of these materials exhibit relatively low electrochemical activity and are hydrophobic, which precludes their use in aquatic conditions. Therefore, it is necessary to identify highly conductive, hydrophilic, and electrocatalytically active catalyst supports to facilitate the design of novel materials with excellent catalytic efficiency.

Research interest has recently been focused on MXenes that are a novel family of metal carbides produced by selectively etching MAX phases. Ti_3C_2 MXene is regarded as the most valuable member of the MXene family. Owing to its unique properties, two-dimensional (2D) Ti_3C_2 MXene has been used in a variety of applications, including supercapacitors, batteries, water-splitting processes, and biomedical applications.[23–26]

Department of Electronics and Information Convergence Engineering, Institute for Wearable Convergence Electronics, Kyung Hee University, 1732 Deogyeong-daero, Giheung-gu, Yongin-si, Gyeonggi-do 17104, Republic of Korea.
E-mail: jsyu@khu.ac.kr

† Electronic supplementary information (ESI) available. See DOI: https://doi.org/10.1039/d4qm00095a

‡ These authors equally contributed to this work.

Ti_3C_2 Mxene has thin atomic layer, high electrical conductivity (9880 S cm^{-1}), hydrophilicity, abundance of active sites, and excellent mechanical properties.[27] When it comes to fine-tuning the overall catalytic water-splitting reaction, 2D Ti_3C_2 MXene is an excellent option for conductive catalytic assistance. For instance, due to the increased proportion of exposed MoS_2 edges and the lower ΔGH^* values, the MoS_2 growth on Ti_3C_2 MXene results in improved electrocatalytic achievement.[28] Therefore, to provide better electrocatalytic materials for the use in HER process, we developed a novel method to produce a synergistic hybrid heterostructured material by fusing the structural characteristics of Ti_3C_2 MXene with the directed growth of NiS and Co_4S_3. With the findings of previous studies,[29] we predicted that using MXene to form a hybrid structure composed of Ti_3C_2 MXene@NiS and Ti_3C_2 MXene@Co_4S_3 would enhance the HER activities of both NiS and Co_4S_3.

In this work, we synthesized the NiS and Co_4S_3 on Ti_3C_2 MXene surfaces *via* hydrothermal synthesis procedures that are easily repeatable. When compared with Ti_3C_2 MXene, the produced Ti_3C_2 MXene@NiS and Ti_3C_2 MXene@Co_4S_3 catalysts exhibited greater catalytic activity about the HER. The overpotentials of the Ti_3C_2 MXene@NiS and Ti_3C_2 MXene@Co_4S_3 catalysts were investigated for the HER. Moreover, fine-tuning the morphology and structure of NiS and Co_4S_3 on the surface of Ti_3C_2 MXene can affect the electron coupling between both NiS and Ti_3C_2 MXene and Co_4S_3 and Ti_3C_2 MXene, thereby enhancing the electron transfer, which leads to an increase in the intrinsic HER activities of the catalysts. The approach used here to enhance a catalyst for the HER offers an opportunity for the future production of excellent TMD catalysts for electrochemical applications.

2. Experimental section

2.1. Materials

The Ti_3AlC_2 (98% powder) used in this experiment was purchased from Aladdin (South Korea). The hydrofluoric acid (HF), ethanol (C_2H_6O), paraffin, nickel nitrate hexahydrate ($Ni(NO_3)_2 \cdot 6H_2O$), and cobalt nitrate hexahydrate ($Co(NO_3)_2 \cdot 6H_2O$) were purchased from Sigma–Aldrich (South Korea). The thiourea (CSN_2H_4) was supplied by Daejung Chemicals (South Korea). The analytic grade of each chemical reagent allowed for use without additional purification.

2.2. Synthesis of multilayer Ti_3C_2 MXene

Typically, 50 mL of 40 wt% HF aqueous solution was gradually filled with 1 g of Ti_3AlC_2 powder and allowed to stand for 48 hours at room temperature (RT). The final product was then continuously washed with deionized water until the pH was neutralized. After collecting it, the produced precipitate (Ti_3C_2 MXene) was dried in a vacuum oven for 10 hours.

2.3. Synthesis of Ti_3C_2 MXene@NiS and Ti_3C_2 MXene@Co_4S_3 hybrid structures

A simple hydrothermal approach was used to synthesize the Ti_3C_2 MXene@NiS and Ti_3C_2 MXene@NiS composites. First, 0.29 g of $Ni(NO_3)_2 \cdot 6H_2O$ was dissolved in 40 mL of deionized water, and the mixture was agitated for 20 min at RT. Additionally, 10 mL of ethanol was mixed with 0.1 g of Ti_3C_2 MXene before being ultrasonically treated for 30 minutes. The above-prepared nickel solution was then quickly mixed with the Ti_3C_2 MXene solution for 20 minutes. The (0.2 g) thiourea was then added and stirred for the following 20 minutes at RT. The Teflon liner was then filled with this solution, which was then kept at 200 °C for 12 hours in a box furnace. After being washed with ethanol and vacuum-dried at 60 °C for 8 hours, Ti_3C_2 MXene@NiS was obtained. In addition, Ti_3C_2 MXene@Co_4S_3 was synthesized in the same way as Ti_3C_2 MXene@NiS, except that $Co(NO_3)_2 \cdot 6H_2O$ (0.29 g) was used in place of $Ni(NO_3)_2 \cdot 6H_2O$ (0.29 g).

2.4. Characterizations

The morphologies and microstructures of the synthesized samples were analyzed by using a field-emission scanning electron microscope (FE-SEM). Transmission electron microscope (TEM) was used to study the intrinsic properties of the prepared material. The crystal structure of the obtained product was characterized by X-ray diffraction (XRD) with a Cu Ka X-ray radiation diffractometer. The surface elements were analyzed by X-ray photoelectron spectroscopy (XPS). Inductively coupled plasma mass spectrometry (ICP-MS) analysis was also used to study elemental composition in the prepared materials.

2.5. Preparation of working electrodes using synthesized materials and commercial 20% Pt/C

The synthesized Ti_3C_2 MXene@NiS (2.5 mg), Ti_3C_2 MXene@Co_4S_3 (2.5 mg), and Ti_3C_2 MXene (2.5 mg), 20% Pt/C, and 5% wt% Nafion (0.1 mL) were ultrasonically mixed into the solution containing deionized water (0.1 mL) and ethanol (0.3 mL). The working electrode was then engineered by drop-casting the 50 μL of the mixed ink onto a piece of carbon paper that was 1 cm × 1 cm in size and air-dried before being subjected to electrochemical experiments.

2.6. Electrochemical measurements

The working electrode was carbon paper supported with all the catalyst materials, whereas the counter and reference electrodes were Pt wire and Hg/HgO, respectively. For comparison, the commercial 20% Pt/C catalyst was also measured. The reversible hydrogen electrode (RHE) was used to convert the observed potentials in this study using the formula $E(\text{RHE}) = E(\text{SCE}) + 0.140 + 0.0591\ \text{pH}$. HER activity of the obtained catalysts was assessed using linear sweep voltammetry (LSV) measurements with a scan rate of 5 mV s^{-1} and 1 M KOH electrolyte. Without *iR* compensation, all the potentials in LSV curves were shown. Electrochemical impedance spectroscopy (EIS) measurements were carried out with a frequency range from 100 kHz to 0.01 Hz at the bias voltage of 5 mV. The chronopotential curve was used to evaluate the durability of the material for 10 hours at a constant current density of 10 mA cm^{-2}.

3. Results and discussion

3.1. Electrocatalyst synthesis and characterization

There are several factors to consider, including crystal phase, morphology, size and shape distributions, surface chemistry, and crystallinity, when synthesizing nanomaterials for electrocatalytic applications.[30] It is important to examine the benefits and drawbacks of the many synthesis methods currently in use, before choosing which approach is suitable for a given application. For instance, the wet-chemical approach produced phases having clear boundaries, but with larger particle sizes.[31] While gas phase methods may create nanosized particles with narrow size distributions, they also need the selection of suitable precursors which may not always be readily available or inexpensive.[32] Furthermore, hydrothermal techniques are more effective for controlling the nano-morphology by modifying reaction parameters such as temperature, pressure, *etc.*, even if they frequently result in introducing defects due to the compaction effects brought on by high temperatures.[33] To produce the necessary electrocatalysts, an essential hydrothermal approach was employed in this study that carefully takes into account each of the characteristics indicated above. MXenes, 2D layered nanomaterials of transition metal carbide, have shown outstanding research output since it was originally published in 2011.[34] Current research focuses on the materials based on transition metals that are developed on MXene surfaces. We used a hydrothermal approach to produce the metal sulfide (NiS and Co_4S_3) grown on the MXene surface. The MAX phase was first etched in HF solution to prepare the MXene, and after that, the MXene as obtained was mixed with the NiS and Co_4S_3 precursors. The solution mixture was then put into a stainless steel autoclave with a Teflon liner so that a hydrothermal reaction took place in a box furnace for 12 hours at 200 °C. Additionally, water and ethanol were used to wash the Ti_3C_2 MXene@NiS and Ti_3C_2 MXene@Co_4S_3 precipitates, followed by drying at 60 °C in a vacuum oven. The synthesis procedure of metal sulfide with Ti_3C_2 MXene hybrid structure as the HER electrocatalyst is schematically illustrated in Scheme 1. First, FE-SEM analysis was used to examine the morphology and intrinsic structure of the hybrid Ti_3C_2 MXene, tTi_3C_2 MXene@NiS, and Ti_3C_2 MXene@Co_4S_3 structures. The bulk MAX thick layered structure was HF etched for 48 h and then, Ti_3C_2 MXene nanosheets were collected following washing, as seen in the FE-SEM images in Fig. 1(a) and (b). The prepared MXene has a large surface area to support enormous NiS and Co_4S_3 nanoparticles. The FE-SEM images revealed an exfoliated, thin, multilayered accordion-like structure due to the homogeneous intercalation of NiS and Co_4S_3 between the Ti_3C_2 MXene layers. As shown in Fig. 1(c) and (d), NiS was grown vertically on the surface of Ti_3C_2 MXene in the form of nanorods. The existence and consistent distribution of Ni, Ti, C, and S elements in the MXene@NiS hybrid structure are shown in Fig. S1(a) (ESI†). Furthermore, Co_4S_3 particles are uniformly dispersed on the surface of Ti_3C_2 MXene in the honeycomb-like structure of the Ti_3C_2 MXene@Co_4S_3 hybrid, as seen in Fig. 1(e) and (f). Co, Ti, C, and S elements are present and are distributed uniformly throughout the Ti_3C_2 MXene@Co_4S_3 hybrid structure, as shown in Fig. S1(b) (ESI†).

Moreover, TEM and high-resolution (HR)-TEM analyses were performed to distinguish the internal morphological properties of the prepared Ti_3C_2 MXene@Co_4S_3 material. The TEM image of Ti_3C_2 MXene@Co_4S_3 nanosheets, which is displayed in Fig. 2(a), revealed the presence of Co_4S_3 particles and their conjugation in ultrathin nanosheets of Ti_3C_2 MXene. This observation provides additional evidence for the accumulation of Co_4S_3 particles on the Ti_3C_2 MXene sheets in the composite material. Also, the Ti_3C_2 MXene@Co_4S_3 nanosheet structure had a significant porous nature. The synthesized material with several nanosheets can deliver more opportunities for ion transport between electrode and electrolyte, which is more favorable for electrocatalytic applications. In addition, in the inverse fast Fourier transform (FFT) image (highlighted in yellow and white colors in the inset of Fig. 2(b)), which is extracted from the HR-TEM image, the edge of the Ti_3C_2 MXene@Co_4S_3 signifies the high crystalline behavior. Using the inverse FFT image (white color), the lattice spacing was determined to be 0.29 nm which corresponds to the Co_4S_3 (100) crystalline plane. Similarly, on the other hand, the lattice

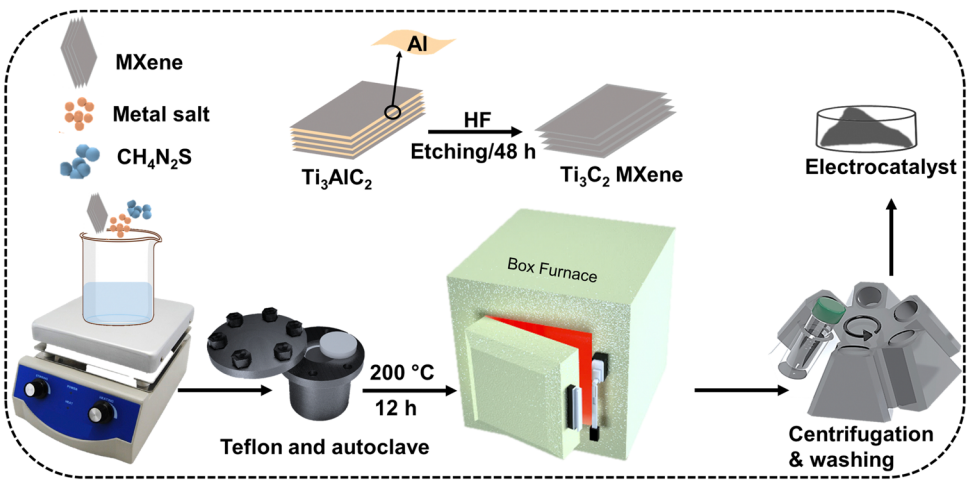

Scheme 1 Schematic illustration for the synthesis process of Ti_3C_2 Mxene composite with Ni/Co sulfide.

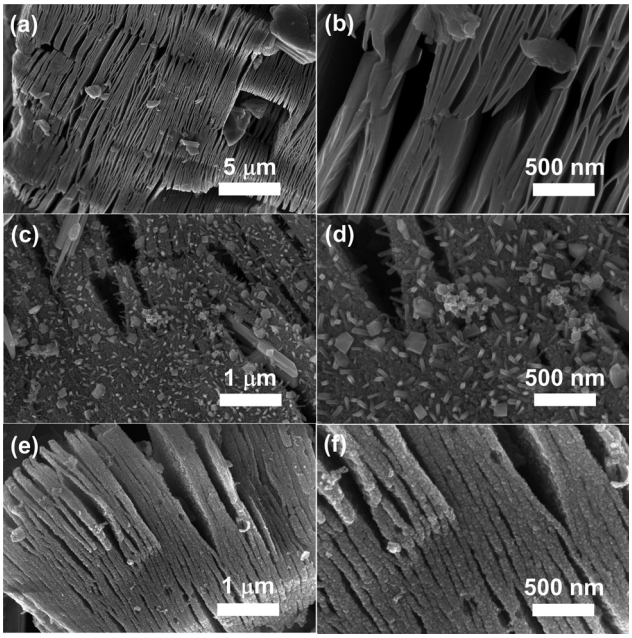

Fig. 1 FE-SEM images of the synthesized (a) and (b) Ti_3C_2 MXene, (c) and (d) Ti_3C_2 MXene@NiS, and (e) end (f) Ti_3C_2 MXene@Co_4S_3 materials at low and high magnifications, showing layered nanosheet-like morphology.

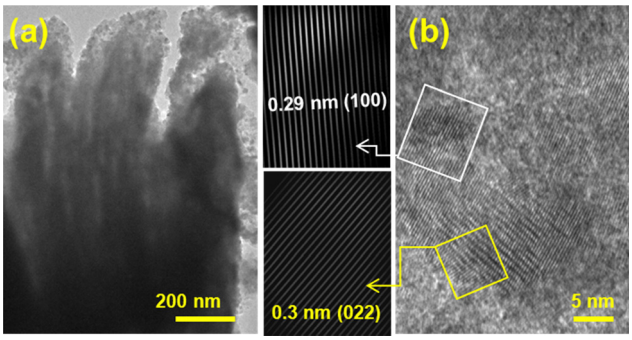

Fig. 2 (a) TEM and (b) HR-TEM images of the Ti_3C_2 MXene@Co_4S_3 composite.

spacing was noticed at 0.3 nm which is related to the Ti_3C_2 MXene (022) crystalline plane (yellow color). The obtained results are well in agreement with the FE-SEM images as shown in Fig. 1(e) and (f).

The crystal structure is also an important parameter for the analysis of the material's phase purity, which can be characterized by using an X-ray diffractometer. As shown in Fig. 3(a), Ti_3C_2 MXene@NiS exhibited the XRD peaks at $2\theta = 18.4^\circ$, 30.3°, 32.2°, 35.8°, 37.6°, 40.6°, 49.2°, 50.3°, 52.8°, 56.4°, and 57.5° that correspond to the (110), (101), (300), (021), (220), (211), (131), (410), (401), (321), and (330) planes of the rhombohedral phase with space group *R*3*m* of NiS (JCPDS no. 003-0760). As shown in Fig. 3(b), XRD was also used to analyze the Ti_3C_2 MXene@Co_4S_3 sample. The 2θ peaks could be observed at 30.5°, 35.3°, 46.7°, and 54.2° corresponding to the (100), (101), (102), and (110) planes of the hexagonal phase with space group *P*63/*mmc* of

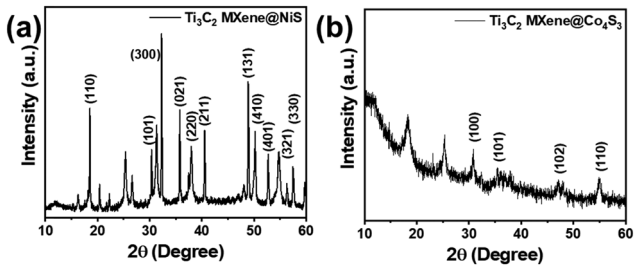

Fig. 3 XRD patterns of the (a) Ti_3C_2 MXene@NiS and (b) Ti_3C_2 MXene@Co_4S_3 materials.

Co_4S_3 (JCPDS no. 002-1458). As shown in Fig. S2 (ESI†), all the obtained major diffraction peaks of Ti_3C_2 Mxene agree well with CCDC no. 96-153-2228. As a result, some of the major diffraction patterns of the prepared Ti_3C_2 MXene catalysts were matched with those of the individual NiS (JCPDS no. 003-0760) and Co_4S_3 (JCPDS no. 002-1458) catalysts, which verifies the successful formation of Ti_3C_2 Mxene@Ni/Co sulfide composites.

In addition, the chemical composition of the synthesized catalysts was examined by X-ray photoelectron spectroscopy (XPS). The XPS survey scan spectrum (Fig. S3(a), ESI†) verified the presence of Ni, Ti, C, and S elements in the prepared Ti_3C_2 MXene@NiS composite. In the Ni 2p spectrum of Fig. 4(a), the Ni $2p_{3/2}$ and Ni $2p_{1/2}$ peaks were located at the energies of 852.9, 855.7, and 870.3 eV, respectively. Ni exists in two states: the metallic state at 852.9 eV and the oxidation state of Ni^{2+} at 855.7 eV, respectively. Additionally, two satellite peaks at 860.3 and 873.8 eV were noticed.[35,36] The Ni–S bond is represented by the peak at 161.2 eV in the S 2p spectrum, while the S^{2-} peak is represented by the peak at 162.8 eV for NiS. The partial S oxidation resulted in the appearance of a satellite peak at 168.2 eV (see Fig. 4(b)).[37] The charge transfer between MXene

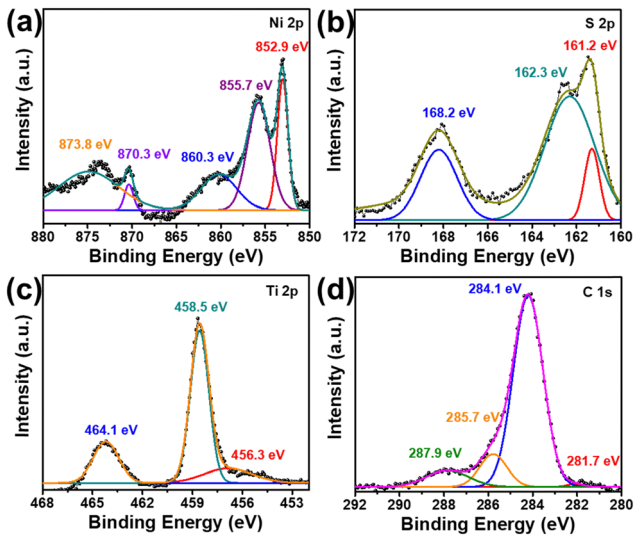

Fig. 4 High-resolution XPS core-level spectra of the Ti_3C_2 MXene@NiS: (a) Ni 2p spectrum, (b) S 2p spectrum, (c) Ti 2p spectrum, and (d) C 1s spectrum.

and nickel sulfide was also demonstrated by the Ti 2p XPS of Ti_3C_2 MXene@NiS. The $2p_{3/2}$ orbits of Ti^{3+} and TiO, respectively, should be associated with the peaks for Ti 2p (see Fig. 4(c)) at 456.3 and 458.5 eV. Additionally, other peaks located at 464.1 eV can be attributed to Ti–C $2p_{1/2}$ and Ti–O $2p_{1/2}$.[38,39] The C–Ti, C–Ti–C, C–C, and C–OH bonds are represented by the four peaks at 281.7, 284.1, 285.7, and 287.9 eV in the high-resolution C 1s XPS spectrum of MXene@NiS (see Fig. 4(d)).[40]

Furthermore, the Ti_3C_2 MXene@Co_4S_3 was also examined by XPS to determine the chemical balancing condition. Fig. S3(b) (ESI†) shows the XPS survey scan spectrum of the Ti_3C_2 MXene@Co_4S_3 material, confirming the existence of Co, Ti, C, and S elements. In Fig. 5(a), the Co 2p spectrum, the Co $2p_{3/2}$, and Co $2p_{1/2}$ peaks were located at 778.2 and 793.5 eV, respectively. The metallic state of Co and the oxidation state of Co^{2+} are denoted, respectively, by the Co $2p_{3/2}$ peak energies of 778.2 and 779.7 eV.[41,42] The Co–S bond can be identified by the peak at 161.7 eV in the S 2p spectrum, while the S^{2-} peak is indicated by the peak at 163.3 eV for the Co_4S_3. The partial S oxidation resulted in the appearance of a satellite peak at 168.2 eV (see Fig. 5(b)).[43] The charge transfer between MXene and cobalt sulfide was also revealed by the Ti 2p XPS of Ti_3C_2 MXene@Co_4S_3. The $2p_{3/2}$ orbits of Ti^{3+} and TiO, respectively, should be associated with the peaks for Ti 2p (Fig. 5(c)) at 455.1 and 458.1 eV. Additionally, TiC $2p_{1/2}$ and TiO $2p_{1/2}$ are responsible for another peak at 463.7 eV.[38,39] The four peaks at 281.2, 284.1, 285.5, and 288.1 eV, which correspond to the C–Ti, C–Ti–C, C–C, and C–OH bonds, may be fitted into the high-resolution C 1s XPS spectra of MXene@Co_4S_3 (see Fig. 5(d)).[40] It was determined that the Ti_3C_2 MXene was effectively decorated with metal sulfide. These XPS data show that the strong covalent networks between NiS/Co_4S_3 and Ti_3C_2 MXene modified the electronic structures of Ti, Co, and Ni and that the heterogeneous interfacial electronic coupling might enhance HER activity.

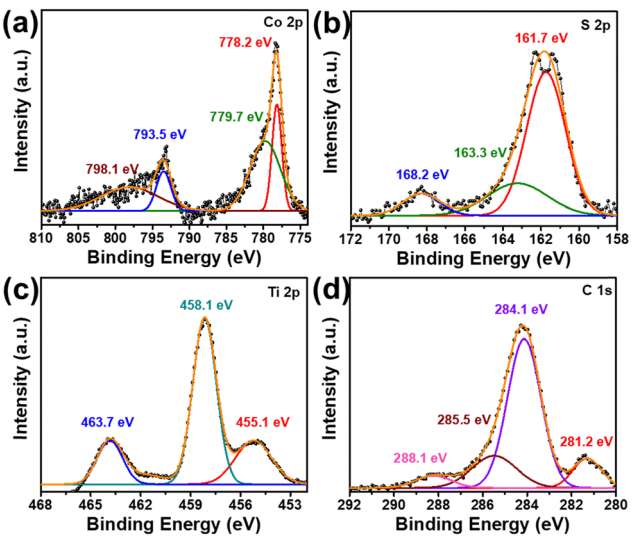

Fig. 5 High-resolution XPS core-level spectra of the Ti_3C_2 MXene@Co_4S_3: (a) Co 2p spectrum, (b) S 2p spectrum, (c) Ti 2p spectrum, and (d) C 1s spectrum.

3.2. Electrocatalytic performance for HER

The LSV measurements of the prepared samples were carried out with a standard three-electrode setup in an alkaline electrolyte (1 M KOH) to assess the HER activities of the electrocatalysts as obtained. All of the synthesized materials utilized as electrocatalysts for HER were coated on carbon paper as a substrate. Furthermore, under the same conditions, the electrocatalytic performances of Ti_3C_2 MXene@NiS, Ti_3C_2 MXene@Co_4S_3, Ti_3C_2 MXene, and 20% Pt/C were examined for comparison. Poor electrocatalytic HER behavior was seen with Ti_3C_2 MXene, as illustrated in Fig. 6(a), which is consistent with the ref. 44. As shown in Fig. 6(b), the Ti_3C_2 MXene@Co_4S_3 had a lower overpotential of 142 mV than the Ti_3C_2 MXene@NiS (173 mV) and Ti_3C_2 MXene (270 mV) to achieve a current density of 10 mA cm^{-2}, exhibiting excellent electrocatalytic HER activity. On the other hand, the increased HER activity for the Ti_3C_2 MXene@Co_4S_3 may be attributed to a uniform distribution of the cobalt sulfide particles throughout the MXene surface, resulting in large number of active sites. In contrast, the inherent activity of Co_4S_3 may be enhanced by the charge transfer caused by Ti_3C_2 MXene. To analyze the electrocatalytic HER kinetics of the catalysts, the Tafel slopes were further computed from the LSV curves (Fig. 6(c)). The Ti_3C_2 MXene@Co_4S_3 had a lowered Tafel slope of 126 mV dec^{-1}, as expected, compared to the Ti_3C_2 MXene@NiS (157 mV dec^{-1}) and Ti_3C_2 MXene (176 mV dec^{-1}), showing fast charger-transfer performance. Moreover, the charge-transfer kinetics were also investigated using EIS measurements (Fig. 6(d)). The Nyquist

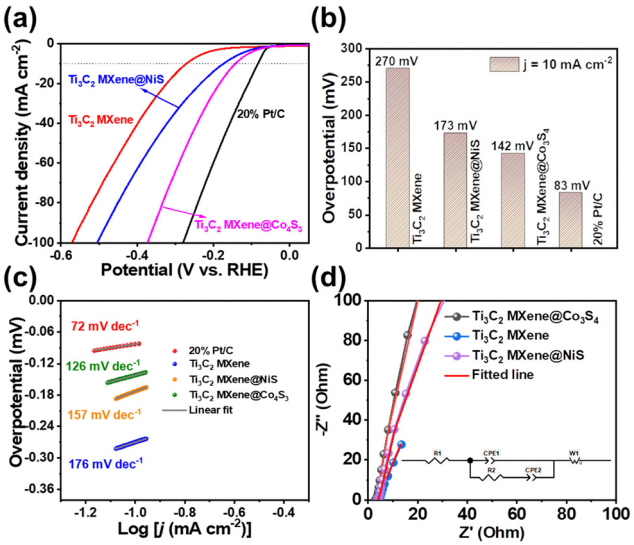

Fig. 6 (a) LSV curves for all the catalyst samples measured at 5 mV s^{-1} in 1 M KOH, (b) overpotential data taken at 10 mA cm^{-2}, and (c) kinetic behavior using Tafel slope curves of 20% Pt/C, Ti_3C_2 MXene, Ti_3C_2 MXene@NiS, and Ti_3C_2 MXene@Co_4S_3. (d) EIS plots of the Ti_3C_2 MXene, Ti_3C_2 MXene@NiS, and Ti_3C_2 MXene@Co_4S_3. The inset of (d) shows an equivalent circuit diagram.

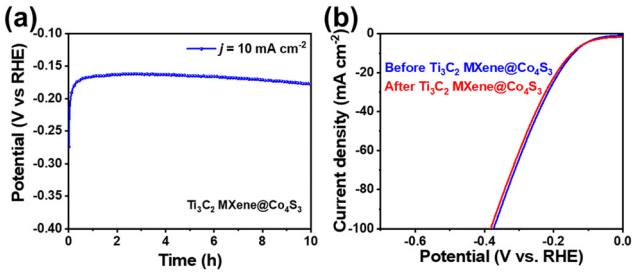

Fig. 7 (a) Long-term stability test result by the CP technique up to 10 h and (b) LVS curves before and after the 10 h CP test for the Ti_3C_2 MXene@Co_4S_3 sample, showing minimal loss of the potential.

plots of the designed Ti_3C_2 Mxene-based catalysts were fitted using Zview software, as shown in the inset of Fig. 6(d). The corresponding equivalent circuit consists of R_1, R_2, CPE, and W_1 parameters which represent an equivalent series resistance, charge-transfer resistance (R_{ct}), constant phase element, and Warburg element, respectively. In comparison to the Ti_3C_2 MXene, the MXene@NiS and Ti_3C_2 MXene@Co_4S_3 were found to have the lowest R_{ct} value, which is in good agreement with the findings of the Tafel slopes. These findings show that the multifunctional Ti_3C_2 MXene support and Co_4S_3 shape can boost intrinsic activity, expose the active site more, and speed up charge transfer. The electrochemical surface area of the electrocatalysts was analyzed using the double-layer capacitance (C_{dl}) to demonstrate the increase in HER activity. To determine the value of C_{dl}, the cyclic voltammetry (CV) tests were performed in the non-faradaic area (Fig. S4(a,c,e), ESI†). The C_{dl} of Ti_3C_2 MXene@Co_4S_3 was 68 μF cm^{-2}, as seen in Fig. S4(f) (ESI†), which is higher than those of Ti_3C_2 MXene@NiS (56 μF cm^{-2} in Fig. S4(d), ESI†) and Ti_3C_2 MXene (17 μF cm^{-2} in Fig. S4(b), ESI†). The larger active surface area of Ti_3C_2 MXene@Co_4S_3 is evident from the higher C_{dl}, which leads to more active sites being exposed and suitable contact with electrolytes.

The chronopotentiometry (CP) test, an additional important measurement of a noteworthy electrocatalyst, was then used to evaluate the electrocatalytic stability of the material. The CP measurement in Fig. 7(a) was first carried out with a constant current density of 10 mA cm^{-2}. Moreover, the long-term durability test for the Ti_3C_2 MXene@NiS and Ti_3C_2 MXene catalysts was also investigated and both materials showed good stability performance (Fig. S5 and S6, ESI†). It is remarkable to note that minimal degradation was observed during continuous operation over time. This suggests that Ti_3C_2 MXene-based catalysts have good conductivity and quick charge transfer during the HER process. The current density remained unchanged during nearly a 10-hour test, indicating the considerable HER durability of Ti_3C_2 MXene@Co_4S_3.[45–48] To harness the overpotential, we also evaluated LSV in Fig. 7(b) after the CP test, which indicates that Ti_3C_2 MXene@Co_4S_3 exhibits the least amount of overpotential loss. To determine the elemental composition, before and after the electrolytic test, the Ti_3C_2@Co_4S_3 catalyst was analyzed by the ICP-MS technique. Before the test, the Ti_3C_2@Co_4S_3 catalyst unveiled a concentration of 2.254×10^4 ppb with a relative standard deviation (RSD) of 1.17%, and cobalt had a concentration of 1.731×10^4 ppb with an RSD of 1.02%. Meanwhile, after the test, the Ti_3C_2@Co_4S_3 catalyst showed a concentration of 2.367×10^3 ppb with an RSD of 0.32%, and cobalt exhibited a concentration of 4.427×10^3 ppb with an RSD of 0.77%. The obtained results confirmed potential alterations in metal concentrations (Co/Ti), which might reflect the formation of Ti_3C_2 MXene@Co_4S_3 composites. Notably, the consistent mass/molar ratios and low variability suggest minimal metal sulfide leaching.

4. Conclusions

In summary, this study involves the synthesis of the multifunctional Ti_3C_2 MXene-supported metal sulfide (NiS and Co_4S_3) directed structures. As a result of its considerable surface area, robust conductivity, and quick charge transport, the resultant Ti_3C_2 MXene@Co_4S_3 catalyst displayed impressive HER activity and exceptional stability over time. Significantly, the shape of Co_4S_3 produces active areas that are easier to reach, and the intriguing Ti_3C_2 MXene support effectively controls the electrical structure. The experimental results, which revealed the 142 mV overpotential to obtain 10 mA cm^{-2} HER activity, showed the strong electronic interaction between Ti_3C_2 MXene and Co_4S_3 as a prediction. From these results, the Ti_3C_2 MXene@Co_4S_3 is expected to be a promising material for application in the HER process. This research provides a new method of producing metal sulfide-based composites with efficient MXene catalysts and clarifies how surface electronic coupling might increase the inherent activity of catalysts.

Conflicts of interest

The authors declare that they have no known competing financial interests or personal relationships that could have appeared to influence the work reported in this paper.

Acknowledgements

This work was supported by a National Research Foundation of Korea (NRF) grant funded by the Korean government (MSIT) (No. 2018R1A6A1A03025708).

References

1 G. W. Crabtree and M. S. Dresselhaus, The Hydrogen Fuel Alternative, *MRS Bull.*, 2008, **33**, 421–428.
2 A. Eftekhari, Electrocatalysts for hydrogen evolution reaction, *Int. J. Hydrog. Energy*, 2017, **42**, 11053–11077.
3 N. Chauhan, H. W. Choi, M. Kumar and D. H. Yoon, Nanoarchitectonic manganese-cobalt phosphide through zeolitic–imidazolate framework for efficient electrocatalysis in hydrogen evolution reaction, *J. Alloys Compd.*, 2022, **926**, 166991.

4 D. Voiry, J. Yang and M. Chhowalla, Recent Strategies for Improving the Catalytic Activity of 2D TMD Nanosheets Toward the Hydrogen Evolution Reaction, *Adv. Mater.*, 2016, **28**, 6197–6206.
5 M. Zeng and Y. Li, Recent advances in heterogeneous electrocatalysts for the hydrogen evolution reaction, *J. Mater. Chem. A*, 2015, **3**, 14942–14962.
6 L. Lin, P. Sherrell, Y. Liu, W. Lei, S. Zhang, H. Zhang, G. G. Wallace and J. Chen, Engineered 2D Transition Metal Dichalcogenides—A Vision of Viable Hydrogen Evolution Reaction Catalysis, *Adv. Energy Mater.*, 2020, **10**, 1903870.
7 I. F. Teixeira, N. V. Tarakina, I. F. Silva, N. López-Salas, A. Savateev and M. Antonietti, Overcoming Electron Transfer Efficiency Bottlenecks for Hydrogen Production in Highly Crystalline Carbon Nitride-Based Materials, *Adv. Sustain. Syst.*, 2022, **6**, 2100429.
8 Y. Zhu, Q. Lin, Y. Zhong, H. A. Tahini, Z. Shao and H. Wang, Metal oxide-based materials as an emerging family of hydrogen evolution electrocatalysts, *Energy Environ. Sci.*, 2020, **13**, 3361–3392.
9 C.-C. Weng, J.-T. Ren and Z.-Y. Yuan, Transition Metal Phosphide-Based Materials for Efficient Electrochemical Hydrogen Evolution: A Critical Review, *ChemSusChem*, 2020, **13**, 3357–3375.
10 H. G. Shiraz, X. Crispin and M. Berggren, Transition metal sulfides for electrochemical hydrogen evolution, *Int. J. Hydrog. Energy*, 2021, **46**, 24060–24077.
11 W. Feng, W. Pang, Y. Xu, A. Guo, X. Gao, X. Qiu and W. Chen, Transition Metal Selenides for Electrocatalytic Hydrogen Evolution Reaction, *ChemElectroChem*, 2020, **7**, 31–54.
12 W. He, L. Han, Q. Hao, X. Zheng, Y. Li, J. Zhang, C. Liu, H. Liu and H. L. Xin, Fluorine-Anion-Modulated Electron Structure of Nickel Sulfide Nanosheet Arrays for Alkaline Hydrogen Evolution, *ACS Energy Lett.*, 2019, **4**, 2905–2912.
13 Y. Zhou, Y. Wu, D. Guo, J. Li, G. Dong, D.-F. Chai, X. Yang, S. Fu and G. Sui, Sulfur vacancy modulated nickel-doped Co_4S_3 hollow nanocube/nitrogen-doped V_2CT_x MXene nanosheet composites for optimizing the hydrogen evolution reaction, *Mater. Chem. Front.*, 2023, **7**, 306–314.
14 H. Zhang, H. Xu, L. Wang, C. Ouyang, H. Liang and S. Zhong, A Metal–Organic Frameworks Derived 1T-MoS_2 with Expanded Layer Spacing for Enhanced Electrocatalytic Hydrogen Evolution, *Small*, 2023, **19**, 2205736.
15 J. Wu, Q. Zhang, K. Shen, R. Zhao, W. Zhong, C. Yang, H. Xiang, X. Li and N. Yang, Modulating Interband Energy Separation of Boron-Doped Fe_7S_8/FeS_2 Electrocatalysts to Boost Alkaline Hydrogen Evolution Reaction, *Adv. Funct. Mater.*, 2022, **32**, 2107802.
16 A. Mondal and A. Vomiero, 2D Transition Metal Dichalcogenides-Based Electrocatalysts for Hydrogen Evolution Reaction, *Adv. Funct. Mater.*, 2022, **32**, 2208994.
17 L. Hu, J. Shi, Z. Peng, Z. Zheng, H. Dong and T. Wang, A high-density nickel–cobalt alloy embedded in nitrogen-doped carbon nanosheets for the hydrogen evolution reaction, *Nanoscale*, 2022, **14**, 6202–6211.
18 Y. Feng, G. Liu, L. Li, J. Ma, C. Zhang and J. Yang, Competitive-Reduction Chemistry on Ni-Doped FeS_2 Catalyst Reinforcing Acid-Corrosion Resistance for Stable Hydrogen Evolution Reactions, *Adv. Energy Sustainability Res.*, 2022, **3**, 2200044.
19 R. Andaveh, G. Barati Darband and M. Maleki, and A. Sabour Rouhaghdam, Superaerophobic/superhydrophilic surfaces as advanced electrocatalysts for the hydrogen evolution reaction: a comprehensive review, *J. Mater. Chem. A*, 2022, **10**, 5147–5173.
20 S. Ali Shah, R. Sayyar, L. Xu, H. Sun, I. Khan, J. Guo, X. Shen, S. Hussain, A. Yuan and H. Ullah, In-situ synthesis of NiS_2 nanoparticles/MoS_2 nanosheets hierarchical sphere anchored on reduced graphene oxide for enhanced electrocatalytic hydrogen evolution reaction, *J. Colloid Interface Sci.*, 2022, **624**, 150–159.
21 X. Zhu, D. C. Nguyen, S. Prabhakaran, D. H. Kim, N. H. Kim and J. H. Lee, Activating catalytic behavior of binary transition metal sulfide-shelled carbon nanotubes by iridium incorporation toward efficient overall water splitting, *Mater. Today Nano*, 2023, **21**, 100296.
22 H. Nolan, C. Schröder, M. Brunet-Cabré, F. Pota, N. McEvoy, K. McKelvey, T. S. Perova and P. E. Colavita, MoS_2/carbon heterostructured catalysts for the hydrogen evolution reaction: N-doping modulation of substrate effects in acid and alkaline electrolytes, *Carbon*, 2023, **202**, 70–80.
23 K. Mistry, Jalja, R. Lakhani, B. Tripathi, S. Shinde and P. Chandra, Recent trends in MXene/Metal chalcogenides for electro-/photocatalytic hydrogen evolution reactions, *Int. J. Hydrog. Energy*, 2022, **47**, 41711–41732.
24 Y. Wei, R. A. Soomro, X. Xie and B. Xu, Design of efficient electrocatalysts for hydrogen evolution reaction based on 2D MXenes, *J. Energy Chem.*, 2021, **55**, 244–255.
25 U. Amara, I. Hussain, M. Ahmad, K. Mahmood and K. Zhang, 2D MXene-Based Biosensing: A Review, *Small*, 2023, **19**, 2205249.
26 E. Kim, J. Song, T.-E. Song, H. Kim, Y.-J. Kim, Y.-W. Oh, S. Jung, I.-S. Kang, Y. Gogotsi, H. Han, C. W. Ahn and Y. Lee, Scalable fabrication of MXene-based flexible micro-supercapacitor with outstanding volumetric capacitance, *J. Chem. Eng.*, 2022, **450**, 138456.
27 X. Wang, T. S. Mathis, K. Li, Z. Lin, L. Vlcek, T. Torita, N. C. Osti, C. Hatter, P. Urbankowski, A. Sarycheva, M. Tyagi, E. Mamontov, P. Simon and Y. Gogotsi, Influences from solvents on charge storage in titanium carbide MXenes, *Nat. Energy*, 2019, **4**, 241–248.
28 Y. Gogotsi and Q. Huang, MXenes: Two-Dimensional Building Blocks for Future Materials and Devices, *ACS Nano*, 2021, **15**, 5775–5780.
29 A. VahidMohammadi, J. Rosen and Y. Gogotsi, The world of two-dimensional carbides and nitrides (MXenes), *Science*, 2021, **372**, eabf1581.
30 J. A. Darr, J. Zhang, N. M. Makwana and X. Weng, Continuous Hydrothermal Synthesis of Inorganic Nanoparticles: Applications and Future Directions, *Chem. Rev.*, 2017, **117**, 11125–11238.

31 H. Zhao, F. Li, S. Wang and L. Guo, Wet Chemical Synthesis of Amorphous Nanomaterials with Well-Defined Morphologies, *Acc. Mater. Res.*, 2021, **2**, 804–815.
32 C. Schulz, T. Dreier, M. Fikri and H. Wiggers, Gas-phase synthesis of functional nanomaterials: Challenges to kinetics, diagnostics, and process development, *Proc. Combust. Inst.*, 2019, **37**, 83–108.
33 G. Yang and S.-J. Park, Conventional and Microwave Hydrothermal Synthesis and Application of Functional Materials: A Review, *Materials*, 2019, **12**, 1177.
34 B. Anasori and Y. Gogotsi, in *2D Metal Carbides and Nitrides (MXenes): Structure, Properties and Applications*, eds. B. Anasori and Y. Gogotsi, Springer International Publishing, Cham, 2019, DOI: 10.1007/978-3-030-19026-2_1, pp. 3–12.
35 M. B. Z. Hegazy, M. R. Berber, Y. Yamauchi, A. Pakdel, R. Cao and U.-P. Apfel, Synergistic Electrocatalytic Hydrogen Evolution in Ni/NiS Nanoparticles Wrapped in Multi-Heteroatom-Doped Reduced Graphene Oxide Nanosheets, *ACS Appl. Mater. Interfaces*, 2021, **13**, 34043–34052.
36 C. Xiong, B. Li, H. Liu, W. Zhao, C. Duan, H. Wu and Y. Ni, A smart porous wood-supported flower-like NiS/Ni conjunction with vitrimer co-effect as a multifunctional material with reshaping, shape-memory, and self-healing properties for applications in high-performance supercapacitors, catalysts, and sensors, *J. Mater. Chem. A*, 2020, **8**, 10898–10908.
37 K. Zhang, Y. Duan, N. Graham and W. Yu, Unveiling the synergy of polymorph heterointerface and sulfur vacancy in NiS/Ni_3S_2 electrocatalyst to promote alkaline hydrogen evolution reaction, *Appl. Catal., B*, 2023, **323**, 122144.
38 T. S. Mathis, K. Maleski, A. Goad, A. Sarycheva, M. Anayee, A. C. Foucher, K. Hantanasirisakul, C. E. Shuck, E. A. Stach and Y. Gogotsi, Modified MAX Phase Synthesis for Environmentally Stable and Highly Conductive Ti_3C_2 MXene, *ACS Nano*, 2021, **15**, 6420–6429.
39 Y. Lee, S. J. Kim, Y.-J. Kim, Y. Lim, Y. Chae, B.-J. Lee, Y.-T. Kim, H. Han, Y. Gogotsi and C. W. Ahn, Oxidation-resistant titanium carbide MXene films, *J. Mater. Chem. A*, 2020, **8**, 573–581.
40 C. Li, D. Zhang, J. Cao, P. Yu, J. Qin and X. Zhang, Ni_3S_2 Nanoparticles Anchored on d-Ti_3C_2 Nanosheets with Enhanced Sodium Storage, *ACS Appl. Energy Mater.*, 2021, **4**, 2593–2599.
41 C. Dong, L. Guo, H. Li, B. Zhang, X. Gao, F. Tian, Y. Qian, D. Wang and L. Xu, Rational fabrication of CoS_2/Co_4S_3@N-doped carbon microspheres as excellent cycling performance anode for half/full sodium ion batteries, *Energy Storage Mater.*, 2020, **25**, 679–686.
42 Q. Peng, X. Shao, C. Hu, Z. Luo, T. Taylor Isimjan, Z. Dou, R. Hou and X. Yang, Co_4S_3 grafted 1 T-phase dominated WS_2 ultrathin nanosheet arrays for highly efficient overall water splitting in alkaline media, *J. Colloid Interface Sci.*, 2022, **615**, 577–586.
43 S. Guo, Y. Li, C. Xue, Y. Sun, C. Wu, G. Shao and P. Zhang, Controllable construction of hierarchically $CdIn_2S_4$/CNFs/Co_4S_3 nanofiber networks towards photocatalytic hydrogen evolution, *J. Chem. Eng.*, 2021, **419**, 129213.
44 R. Zhang, Y. Sun, F. Jiao, L. Li, D. Geng and W. Hu, MXene-MoS_2 nanocomposites via chemical vapor deposition with enhanced electrocatalytic activity for hydrogen evolution, *Nano Res.*, 2023, **16**, 8937–8944.
45 N. Chauhan, H. W. Choi, M. Kumar and D. H. Yoon, Nanoarchitectonics Pt/NiCo in a carbon matrix as highly efficient electrocatalyst for hydrogen evolution reaction, *Electrochim. Acta*, 2023, **460**, 142634.
46 M. Kumar, D. In Jeong, N. Sarwar, S. Dutta, N. Chauhan, S. A. Han, J. Ho Kim and D. Ho Yoon, Cobalt supported nitrogen-doped carbon nanotube as efficient catalyst for hydrogen evolution reaction and reduction of 4-nitrophenol, *Appl. Surf. Sci.*, 2022, **572**, 151450.
47 D. I. Jeong, H. W. Choi, S. Woo, J. H. Yoo, D. Kang, S. Kim, B. Lim, J. H. Kim, S.-W. Kim and B. K. Kang, Electronic structure modification and N-doped carbon shell nanoarchitectonics of Ni_3FeN@NC for overall water splitting performance evaluation, *J. Mater. Chem. A*, 2022, **10**, 16704–16713.
48 B. K. Kang, S. Y. Im, J. Lee, S. H. Kwag, S. B. Kwon, S. Tiruneh, M.-J. Kim, J. H. Kim, W. S. Yang, B. Lim and D. H. Yoon, *In-situ* formation of MOF derived mesoporous Co_3N/amorphous N-doped carbon nanocubes as an efficient electrocatalytic oxygen evolution reaction, *Nano Res.*, 2019, **12**, 1605–1611.